

SELF-SUPERVISED HIGH DYNAMIC RANGE IMAGING WITH MULTI-EXPOSURE IMAGES IN DYNAMIC SCENES

Zhilu Zhang¹, Haoyu Wang¹, Shuai Liu, Xiaotao Wang, Lei Lei, Wangmeng Zuo^{1,*}

¹ Harbin Institute of Technology, Harbin, China

cszllzhang@outlook.com, cshy2002@gmail.com, wmzuo@hit.edu.cn

ABSTRACT

Merging multi-exposure images is a common approach for obtaining high dynamic range (HDR) images, with the primary challenge being the avoidance of ghosting artifacts in dynamic scenes. Recent methods have proposed using deep neural networks for deghosting. However, the methods typically rely on sufficient data with HDR ground-truths, which are difficult and costly to collect. In this work, to eliminate the need for labeled data, we propose SelfHDR, a self-supervised HDR reconstruction method that only requires dynamic multi-exposure images during training. Specifically, SelfHDR learns a reconstruction network under the supervision of two complementary components, which can be constructed from multi-exposure images and focus on HDR color as well as structure, respectively. The color component is estimated from aligned multi-exposure images, while the structure one is generated through a structure-focused network that is supervised by the color component and an input reference (*e.g.*, medium-exposure) image. During testing, the learned reconstruction network is directly deployed to predict an HDR image. Experiments on real-world images demonstrate our SelfHDR achieves superior results against the state-of-the-art self-supervised methods, and comparable performance to supervised ones. Codes are available at <https://github.com/cszhilu1998/SelfHDR>.

1 INTRODUCTION

Scenes with wide brightness ranges are often visible to human observers, but capturing them completely with digital or smartphone cameras can be arduous due to the restricted dynamic range of sensors. For instance, during sunset, the sun and sky are substantially brighter than the surrounding landscape, leading the camera sensor to either over-expose the sky or under-expose the landscape. To obtain high dynamic range (HDR) photos in these conditions, exposure bracketing technology becomes a popular option. It captures multiple low dynamic range (LDR) images with varying exposures, which are then merged into an HDR result (Debevec & Malik, 2008; Mertens et al., 2009).

Unfortunately, when the multi-exposure images are misaligned due to camera shake and object movement, ghosting artifacts may exist in the result. Traditional methods to remove the ghosting include rejecting misaligned areas (Zhang & Cham, 2011; Lee et al., 2014; Oh et al., 2014; Yan et al., 2017), aligning input images (TOMASZEWSKA, 2007; Hu et al., 2013; Yan et al., 2019b), and using patch-based composite (Sen et al., 2012; Hu et al., 2013; Ma et al., 2017). With the development of deep learning (He et al., 2016; Dosovitskiy et al., 2020; Liu et al., 2021), recent advances (Kalantari et al., 2017; Wu et al., 2018; Yan et al., 2019a; Liu et al., 2022; Yan et al., 2023a; Tel et al., 2023) proposed training deep neural networks (DNN) for deghosting in a data-driven supervised manner, performing more effectively than traditional ones.

However, DNN-based HDR reconstruction methods usually require sufficient labeled data, each of which should include the input dynamic multi-exposure images and the corresponding HDR ground-truth (GT) image. In order to ensure position alignment between the input reference (*e.g.*, medium-exposure) frame and GT, previous works (Kalantari et al., 2017; Chen et al., 2021; Liu et al., 2023) generally capture the dynamic inputs with the controllable object (generally a person)

*Corresponding author.

motion in a static background, and construct GT by merging static multiple-exposure images of the reference scene. Such a collection process is cumbersome and involves high time as well as labor costs, thus limiting the number and diversity of the datasets. To alleviate the need for labeled data, FSHDR (Prabhakar et al., 2021) and SAME (Yan et al., 2023b) explore a few-shot manner, and Nazarczuk *et al.* (Nazarczuk et al., 2022) introduce a fully self-supervised approach. The main idea is to construct pseudo-pairs for HDR reconstruction. Nevertheless, the performance of these methods is unsatisfactory, as their simulated pairs still have gaps with real-world ones.

In this work, we aim to reconstruct HDR images directly with real-world multi-exposure images in a self-supervised manner, without synthesizing any pseudo-input data. This objective should be feasible, as most of the information required for HDR results can derive from input data. The property will be more intuitive when HDR color and structure are observed, respectively. Specifically, HDR color knowledge can be inferred from aligned multi-exposure images, and HDR structure can be extracted from some one of the inputs.

We further propose SelfHDR, a self-supervised method for HDR image reconstruction. Inspired by the above data characteristics, SelfHDR decomposes the latent HDR GT into available color and structure components, and then takes them to supervise the learning of the reconstruction network. On the one hand, the color component is estimated from multi-exposure images aligned by optical flow. On the other hand, the structure component is generated by feeding aligned inputs into a structure-focused network, which is learned under the supervision of the color component and an input reference (*e.g.*, medium-exposure) image. Moreover, during the training phase of structure-focused and reconstruction networks, elaborate masks are embedded into loss functions to circumvent harmful information in supervision. During inference, only the reconstruction network is required to predict the HDR result from unseen multi-exposure images.

We evaluate the proposed self-supervised methods using four existing HDR reconstruction networks, respectively. The models are trained on Kalantari *et al.* dataset (Kalantari et al., 2017), and tested on multiple datasets (Kalantari et al., 2017; Sen et al., 2012; Tursun et al., 2016). The results show our SelfHDR obtains 1.58 dB PSNR gain compared to the state-of-the-art self-supervised method that uses the same reconstruction network, and achieves comparable performance to supervised ones, especially in terms of visual effects. Besides, we conduct extensive and comprehensive ablation studies, analyzing the effectiveness of different components and variants.

To sum up, the main contributions of this work include:

- We propose a self-supervised HDR reconstruction method named SelfHDR, which learns an HDR reconstruction network by decomposing latent ground-truth into constructible color and structure component supervisions.
- The color component is estimated from aligned multi-exposure images, while the structure one is generated using a structure-focused network supervised by the color component and an input reference image.
- Experiments show that our SelfHDR outperforms the state-of-the-art self-supervised methods, and achieves comparable performance to supervised ones.

2 RELATED WORK

2.1 SUPERVISED HDR IMAGING WITH MULTI-EXPOSURE IMAGES

The main challenge of HDR imaging with multi-exposure images is to avoid ghosting artifacts. DNN-based HDR deghosting methods have exhibited a more satisfactory ability than traditional ones. For the first time, Kalanrati *et al.* (Kalantari et al., 2017) collect a real-world dataset and propose a data-driven convolutional neural network (CNN) approach to merge LDR images aligned by optical flow. Wu *et al.* (Wu et al., 2018) utilize the multiple encoders and one decoder architecture to handle image misalignment, discarding the optical flow. Yan *et al.* (Yan et al., 2019a) present a spatial attention mechanism for deghosting. In addition, we recommend Wang *et al.*'s survey (Wang & Yoon, 2021) for more CNN-based HDR reconstruction methods (Prabhakar et al., 2019; Niu et al., 2021).

Recently, with the development of Transformer (Dosovitskiy et al., 2020; Liu et al., 2021), some works (Liu et al., 2022; Song et al., 2022; Yan et al., 2023a; Tel et al., 2023) bring in self- and

cross-attention to alleviate the ghosting artifacts. For example, Liu *et al.* (Liu *et al.*, 2022) propose HDR-Transformer, which embeds a local context extractor into SwinIR (Liang *et al.*, 2021) basic block for jointly capturing global and local dependencies. Song *et al.* (Song *et al.*, 2022) suggest selectively applying the transformer and CNN model to misaligned and aligned areas, respectively. However, both CNN- and Transformer-based methods require sufficient labeled data for training networks, while the data collection is time-consuming and laborious.

2.2 FEW-SHOT AND SELF-SUPERVISED HDR IMAGING WITH MULTI-EXPOSURE IMAGES

To alleviate the reliance on HDR ground-truths, few-shot and self-supervised HDR reconstruction methods have been explored. FSHDR (Prabhakar *et al.*, 2021) combines unlabeled dynamic samples with few labeled samples to train a neural network, then leverages the model output of unlabeled samples as a pseudo-HDR to generate pseudo-LDR images. Ultimately the HDR reconstruction network is learned with synthetic pseudo-pairs. Nazarczuk *et al.* (Nazarczuk *et al.*, 2022) select well-exposure LDR patches as pseudo-HDR to generate pseudo-LDR, while the static LDR patches are directly merged for HDR ground-truths. However, due to unrealistic motion and illumination in synthetic LDR images, such methods exhibit performance gaps compared to supervised ones. Recently, SAME (Yan *et al.*, 2023b) generates saturated regions in a self-supervised manner first, and then performs dehazing via a semi-supervised framework. But it still has limited performance improvement. In this work, we take full advantage of the internal characteristics of multi-exposure images to present a self-supervised approach SelfHDR, which achieves comparable performance to supervised ones.

Furthermore, some works incorporate emerging techniques to investigate self-supervised HDR reconstruction. For instance, GDP (Fei *et al.*, 2023) exploits multi-exposure images to guide the denoising process of pre-trained diffusion generative models (Ho *et al.*, 2020; Song *et al.*, 2021), reconstructing HDR image. Mildenhall *et al.* (Mildenhall *et al.*, 2022), Jun *et al.* (Jun-Seong *et al.*, 2022), and Huang *et al.* (Huang *et al.*, 2022) employ NeRF (Mildenhall *et al.*, 2020) to synthesize HDR images and the novel HDR views. However, these methods are less practical, since the specific models need to be re-optimized when facing new scenarios.

3 METHOD

3.1 MOTIVATION AND OVERVIEW

Revisit Supervised HDR Reconstruction. The combination of multi-exposure images enables HDR imaging in scenes with a wide range of brightness levels. In static scenes, the HDR image can be easily generated through a weighted sum of multi-exposure images (Debevec & Malik, 2008). However, when applying this approach in dynamic scenes, it will lead to ghosting artifacts. As a result, several recent works (Kalantari *et al.*, 2017; Yan *et al.*, 2019a; Liu *et al.*, 2022; Tel *et al.*, 2023) have suggested learning a deep neural network in a supervised manner for dehazing. Concretely, denote the LDR image taken with exposure time t_i by I_i , where $i = 1, 2, 3$ and $t_1 < t_2 < t_3$. They first map the LDR images to the linear domain, which can be written as,

$$\mathbf{H}_i = \mathbf{I}_i^\gamma / t_i, \quad (1)$$

where γ denotes the gamma correction parameter and is generally set to 2.2. Then they concatenate I_i and \mathbf{H}_i , feeding them to the reconstruction network \mathcal{R} with parameters $\Theta_{\mathcal{R}}$, *i.e.*,

$$\hat{\mathbf{Y}} = \mathcal{R}(\mathbf{X}_1, \mathbf{X}_2, \mathbf{X}_3; \Theta_{\mathcal{R}}), \quad (2)$$

where $\mathbf{X}_i = \{I_i, \mathbf{H}_i\}$, $\hat{\mathbf{Y}}$ denotes the reconstructed HDR image. The optimized network parameters can be obtained by the following formula,

$$\Theta_{\mathcal{R}}^* = \arg \min_{\Theta_{\mathcal{R}}} \mathcal{L}(\mathcal{T}(\hat{\mathbf{Y}}), \mathcal{T}(\mathbf{Y})), \quad (3)$$

where \mathcal{L} represents the loss function, \mathbf{Y} denotes the HDR GT image. \mathcal{T} is the tone-mapping process, represented as,

$$\mathcal{T}(\mathbf{Y}) = \frac{\log(1 + \mu\mathbf{Y})}{\log(1 + \mu)}, \text{ where } \mu = 5,000. \quad (4)$$

Motivation of SelfHDR. The acquisition of labeled data for HDR reconstruction is usually time-consuming and laborious. To alleviate the requirement of HDR GT, some works (Prabhakar et al., 2021; Yan et al., 2023b; Nazarczuk et al., 2022) have explored few-shot and zero-shot HDR reconstruction by constructing pseudo-pairs. However, their performance is unsatisfactory due to the gaps between the simulated pairs and real-world ones, especially in a fully self-supervised manner.

In this work, we expect to get rid of the demand for synthetic data, achieving self-supervised HDR reconstruction directly with real-world dynamic multi-exposure images. The goal should be feasible, as the multi-exposure images have provided probably sufficient information for HDR reconstruction. The property will be more intuitive when the color and structure are observed, respectively. On the one hand, the color of HDR images can be estimated from aligned inputs. On the other hand, the structure information of the HDR images can be generally discovered in some one of multi-exposure images, *i.e.*, most textures exist in the medium-exposure image, dark details are obvious in the high-exposure one, and bright scenes are clearly visible in the low-exposure one.

What we need to do is to dig for the right information from the multi-exposure images for constructing the HDR image. However, it is actually difficult to explore a straightforward self-supervised method that generates HDR images directly. Considering the above properties of HDR color and structure, we treat the two components respectively for ease of self-supervised implementation. Note that it can be a focus or emphasis on color and structure relatively, not necessarily an absolute separation.

Specifically, when training a self-supervised HDR reconstruction network with given multi-exposure images as input, suitable supervision signals have to be prepared. Instead of looking for a complete HDR image, we construct the color and structure components of the supervision respectively (see Sec. 3.2). Then we learn the network under the guidance of both components (see Sec. 3.3).

3.2 CONSTRUCTING COLOR AND STRUCTURE COMPONENTS

3.2.1 CONSTRUCTING COLOR COMPONENT

The color component should represent the HDR color as faithfully as possible, and it can be estimated by fusing the aligned multi-exposure images. Multiple frames in dynamic scenes are generally not aligned caused by camera shake or object motion. Although sometimes a few regions are aligned well, they are not enough to generate acceptable color components. In view

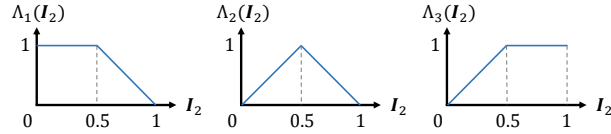


Figure 1: The triangle function that we use as the blending weights to generate color components.

of the effective capabilities of the optical flow estimation method (Liu et al., 2009), it is a natural idea to perform pre-alignment first. Concretely, taking the medium-exposure image I_2 as the reference, we calculate the optical flow from I_2 to I_1 and I_3 , respectively. Thus, we can back warp H_1 and H_3 according to the calculated optical flow, obtaining \tilde{H}_1 and \tilde{H}_3 that are roughly aligned with H_2 . Then we can predict the color component Y_{color} with the following formula,

$$Y_{color} = \frac{A_1 \tilde{H}_1 + A_2 H_2 + A_3 \tilde{H}_3}{A_1 + A_2 + A_3}, \quad (5)$$

where A_i represents pixel-level fusion weight. We follow Kalantari *et al.* (Kalantari et al., 2017) and express A_i as,

$$A_1 = 1 - \Lambda_1(I_2), \quad A_2 = \Lambda_2(I_2), \quad A_3 = 1 - \Lambda_3(I_2), \quad (6)$$

where $\Lambda_i(I_2)$ is shown in Fig. 1.

When the images are perfectly aligned, the color components Y_{color} can be regarded as an HDR image directly. However, such an ideal state is hard to reach due to object occlusion and sometimes non-robust optical flow model. Small errors during pre-alignment may cause blurring, while large ones cause ghosting in color components. Nevertheless, regardless of the ghosting areas, the rest can record the rough color value, and in which well-aligned ones can offer both good color and structure cues of HDR images. Moreover, for the areas with alignment errors, we further construct structure components to guide the reconstruction network in the next subsection.

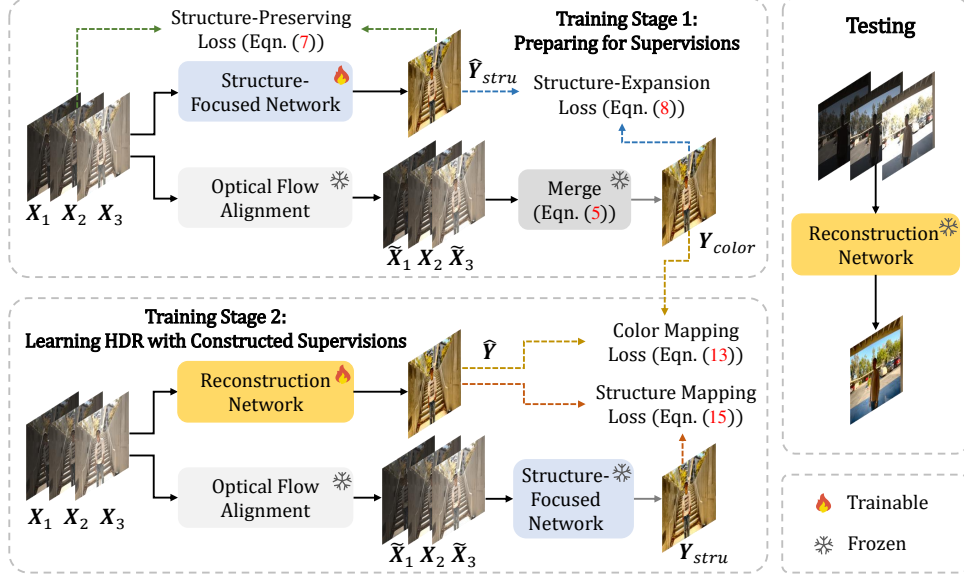


Figure 2: Overview of SelfHDR. During training, we first construct color and structure components (*i.e.*, Y_{color} and Y_{stru}), then take Y_{color} and Y_{stru} for supervising the HDR reconstruction network. During testing, the HDR reconstruction network can be used to predict HDR images from unseen multi-exposure images. Dotted lines with different colors represent different loss terms.

3.2.2 CONSTRUCTING STRUCTURE COMPONENT

Although the medium-exposure image can provide most of the texture information, it is not optimal to take it as the only structure guidance for the HDR reconstruction, as the dark areas may be unclear and over-exposed ones may exist in it. Besides, it is not easy to put into practice when using the low-exposure and high-exposure images as guidance, due to the position and color differences between the HDR image and them. Fortunately, the previously constructed color component Y_{color} can preserve the structure of dark and over-exposed areas to some extent. Therefore, we can combine the medium-exposure image and color component Y_{color} to help construct the structure component.

Concretely, we first learn a structure-focused network with the guidance of medium-exposure image and color component Y_{color} . During training, the network takes the multi-exposure images as input, as shown in Fig. 2. On the one hand, the medium-exposure image guides the network to preserve well-exposed textures from the input reference image. It is accomplished by a structure-preserving loss \mathcal{L}_{sp} , which can be written as,

$$\mathcal{L}_{sp}(\hat{Y}_{stru}, H_2) = \|(\mathcal{T}(\hat{Y}_{stru}) - \mathcal{T}(H_2)) * M_{sp}\|_1, \quad (7)$$

where \hat{Y}_{stru} denotes the network output. M_{sp} emphasizes the well-exposed areas, and mitigates the adverse effects of dark and over-exposed ones in the reference image H_2 . The function $\Lambda_2(I_2)$ (see Fig. 1) can do just that, so we set M_{sp} to $\Lambda_2(I_2)$. On the other hand, the color component Y_{color} guides the network to learn the structure from non-reference images by calculating structure-expansion loss \mathcal{L}_{se} , which can be written as,

$$\mathcal{L}_{se}(\hat{Y}_{stru}, Y_{color}) = \|(\mathcal{T}(\hat{Y}_{stru}) - \mathcal{T}(Y_{color})) * M_{se}\|_1. \quad (8)$$

M_{se} is a binary mask, distinguishing whether the pixel of Y_{color} is composited from well-aligned multi-exposure ones. We design each pixel M_{se}^p of M_{se} as,

$$M_{se}^p = \begin{cases} 1 & |((\mathcal{T}(Y_{color}) - \mathcal{T}(H_2)) * \Lambda_2(I_2))^p| < \sigma_{se} \\ 0 & |((\mathcal{T}(Y_{color}) - \mathcal{T}(H_2)) * \Lambda_2(I_2))^p| \geq \sigma_{se} \end{cases}, \quad (9)$$

where σ_{se} is a threshold and set to $5/255$. In short, the parameter Θ_S of structure-focused network \mathcal{S} is jointly optimized by structure-preserving and structure-expansion loss terms, *i.e.*,

$$\Theta_S^* = \arg \min_{\Theta_S} [\mathcal{L}_{se}(\hat{Y}_{stru}, Y_{color}) + \lambda_{sp} \mathcal{L}_{sp}(\hat{Y}_{stru}, H_2)], \quad (10)$$

where λ_{sp} denotes the weight coefficient of structure-preserving loss and is set to 4.

Then, we feed aligned multi-exposure images rather than original ones into the pre-trained structure-focused network \mathcal{S} . The final structure component \mathbf{Y}_{stru} can be expressed as,

$$\mathbf{Y}_{stru} = \mathcal{S}(\tilde{\mathbf{X}}_1, \mathbf{X}_2, \tilde{\mathbf{X}}_3; \Theta_S^*), \quad (11)$$

where $\tilde{\mathbf{X}}_1$ and $\tilde{\mathbf{X}}_3$ denote aligned \mathbf{X}_1 and \mathbf{X}_3 with the reference of \mathbf{X}_2 . Such an operation can help structure-focused networks reduce the alignment burden, thus further enhancing the structure component. In addition, benefiting from the supervision of the color component, the structural component \mathbf{Y}_{stru} also has some color cues, although it mainly focuses on the HDR textures.

3.3 LEARNING HDR WITH COLOR AND STRUCTURE COMPONENTS

With the color and structure components as guidance, we can train an HDR reconstruction network \mathcal{R} without other ground-truths. The optimized network parameters $\Theta_{\mathcal{R}}^*$ can be modified from Eqn. (3) to the following formula,

$$\Theta_{\mathcal{R}}^* = \arg \min_{\Theta_{\mathcal{R}}} [\mathcal{L}_{color}(\hat{\mathbf{Y}}, \mathbf{Y}_{color}) + \lambda_{stru} \mathcal{L}_{stru}(\hat{\mathbf{Y}}, \mathbf{Y}_{stru})], \quad (12)$$

where $\hat{\mathbf{Y}}$ represents the network output. \mathcal{L}_{color} and \mathcal{L}_{stru} denote color mapping and structure mapping loss terms, respectively. λ_{stru} is the weight coefficient of \mathcal{L}_{stru} and is set to 1.

For color mapping term, we adopt ℓ_1 loss, which can be written as,

$$\mathcal{L}_{color}(\hat{\mathbf{Y}}, \mathbf{Y}_{color}) = \|(\mathcal{T}(\hat{\mathbf{Y}}) - \mathcal{T}(\mathbf{Y}_{color})) * \mathbf{M}_{color}\|_1, \quad (13)$$

where \mathbf{M}_{color} is similar as \mathbf{M}_{se} , and is also a binary mask. It excludes areas where optical flow is estimated incorrectly when generating \mathbf{Y}_{color} . Instead of using Eqn. (9), here we can utilize \mathbf{Y}_{stru} to design a more accurate mask, which can be expressed as,

$$\mathbf{M}_{color}^p = \begin{cases} 1 & |(\mathcal{T}(\mathbf{Y}_{color}) - \mathcal{T}(\mathbf{Y}_{stru}))^p| < \sigma_{color} \\ 0 & |(\mathcal{T}(\mathbf{Y}_{color}) - \mathcal{T}(\mathbf{Y}_{stru}))^p| \geq \sigma_{color} \end{cases}, \quad (14)$$

where p denotes a pixel, σ_{color} is a threshold and set to 10/255. For structure mapping term, we adopt VGG-based (Simonyan & Zisserman, 2015) perceptual loss, which can be written as,

$$\mathcal{L}_{stru}(\hat{\mathbf{Y}}, \mathbf{Y}_{stru}) = \sum_k \|\phi_k(\mathcal{T}(\hat{\mathbf{Y}})) - \phi_k(\mathcal{T}(\mathbf{Y}_{stru}))\|_1, \quad (15)$$

where $\phi_k(\cdot)$ denotes the output of k -th layer in VGG (Simonyan & Zisserman, 2015) network.

4 EXPERIMENTS

4.1 IMPLEMENTATION DETAILS

Framework Details. Note that this work does not focus on the design of network architectures, and we employ existing ones directly. The structure-focused and reconstruction networks use the same architecture. And we adopt CNN-based (*i.e.*, AHDRNet (Yan et al., 2019a) and FSHDR (Prabhakar et al., 2021)) and Transformer-based (*i.e.*, HDR-Transformer (Liu et al., 2022), and SCTNet (Tel et al., 2023)) networks for experiments, respectively. Besides, the optical flow is calculated by Liu et al. (Liu et al., 2009)’s approach, as recommended in (Kalantari et al., 2017; Prabhakar et al., 2021).

Datasets. Experiments are mainly conducted on Kalantari et al. dataset (Kalantari et al., 2017), which are extensively utilized in previous works. The dataset consists of 74 samples for training and 15 for testing. Each sample comprises three LDR images, captured at exposure values of $\{-2, 0, 2\}$ or $\{-3, 0, 3\}$, alongside a corresponding HDR GT image. We use these testing images for both quantitative and qualitative evaluations. Additionally, following (Kalantari et al., 2017; Yan et al., 2019a; Liu et al., 2022), we take the Sen et al. (Sen et al., 2012) and Tursun et al. (Tursun et al., 2016) datasets (without GT) for further qualitative comparisons.

Training Details. The structure-focused and reconstruction networks are trained successively, and share the same settings. The training patches of size 128×128 are randomly cropped from the original images. The batch size is set to 16. Adam (Kingma & Ba, 2015) with $\beta_1 = 0.9$ and $\beta_2 = 0.999$ is

Table 1: Quantitative results on Kalantari *et al.* dataset (Kalantari et al., 2017). ‘SelfHDR_{network}’ denotes the reconstruction network we use, *i.e.*, AHDRNet (Yan et al., 2019a), FSHDR (Prabhakar et al., 2021), HDR-Transformer (Liu et al., 2022), and SCTNet (Tel et al., 2023). The best results in each category are **bolded**.

	Method	PSNR- <i>u</i> / SSIM- <i>u</i>	PSNR- <i>l</i> / SSIM- <i>l</i>	HDR-VDP-2
Fully-Supervised	AHDRNet (CVPR 2019)	43.63 / 0.9900	41.14 / 0.9702	64.61
	FSHDR (CVPR 2021)	43.03 / 0.9902	42.27 / 0.9889	64.79
	HDR-Transformer (ECCV 2022)	44.21 / 0.9918	42.17 / 0.9889	64.63
	SCTNet (ICCV 2023)	44.48 / 0.9916	42.00 / 0.9897	64.47
Few (K)-Shot	FSHDR _{K=5} (CVPR 2021)	43.02 / 0.9874	41.98 / 0.9885	64.54
	FSHDR _{K=1} (CVPR 2021)	42.52 / 0.9846	41.92 / 0.9887	64.41
Self-Supervised	FSHDR _{K=0} (CVPR 2021)	42.17 / 0.9828	41.47 / 0.9884	64.21
	Nazarczuk <i>et al.</i> (ArXiv 2022)	42.15 / -	40.54 / -	63.99
	Our SelfHDR _{AHDRNet}	43.68 / 0.9901	41.09 / 0.9873	64.57
	Our SelfHDR _{FSHDR}	43.75 / 0.9903	42.00 / 0.9881	64.69
	Our SelfHDR _{HDR-Transformer}	43.94 / 0.9907	41.79 / 0.9883	64.98
	Our SelfHDR _{SCTNet}	43.95 / 0.9907	41.77 / 0.9889	64.77

taken to optimize models for 150 epochs. The learning rate is initially set to 1×10^{-4} for CNN-based networks and 2×10^{-4} for Transformer-based ones, and reduces by half every 50 epochs.

Evaluation Configurations. We use peak signal-to-Noise ratio (PSNR), SSIM (Wang et al., 2004), and HDR-VDP-2 (Mantiuk et al., 2011) as evaluation metrics. PSNR and SSIM are both calculated on the linear and tone-mapped domains, denoted as ‘*l*’ and ‘*u*’, respectively.

4.2 COMPARISON WITH STATE-OF-THE-ARTS

As described in Sec. 4.1, we adopt four existing HDR reconstruction networks (*i.e.*, AHDRNet, FSHDR, HDR-Transformer, and SCTNet) for experiments, respectively. We compare them with the corresponding supervised manners and two self-supervised methods (*i.e.*, FSHDR_{K=0} and Nazarczuk *et al.* (Nazarczuk et al., 2022)). And the results of few-shot FSHDR are also provided.

Quantitative Results. Table 1 shows the quantitative comparison results. As loss functions are always calculated on tone-mapped images, and HDR images are typically viewed on LDR displays, we suggest taking evaluation metrics in the tone-mapped domain (*i.e.*, PSNR-*u* and SSIM-*u*) as the primary reference. From the table, four SelfHDR versions all outperform the previous self-supervised methods. Especially, with the same reconstruction network, our SelfHDR_{FSHDR} achieves 1.58 dB PSNR gain than FSHDR_{K=0}. The results of SelfHDR can be further improved with the use of more advanced reconstruction networks (*i.e.*, HDR-Transformer and SCTNet). Moreover, in comparison with the corresponding supervised methods, SelfHDR has comparable performance overall.

Qualitative Results. The visual comparisons on Kalantari *et al.* dataset (Kalantari et al., 2017) as well as Sen *et al.* (Sen et al., 2012) and Tursun *et al.* (Tursun et al., 2016) datasets are shown in Fig. 3 and Fig. 4, respectively. Our results have fewer artifacts than FSHDR_{K=0}, and sometimes even outperform the corresponding supervised methods. They show the same trend as the quantitative ones. Please see the appendix for more results.

5 ABLATION STUDY

The ablation studies are all conducted using AHDRNet (Yan et al., 2019a) as the structure-focused and reconstruction network.

5.1 EFFECT OF COLOR AND STRUCTURE SUPERVISION

The quantitative results of color and structure components (Y_{color} and Y_{stru}) are given in Table 2. From the table, the final HDR results achieve better performance than both Y_{color} and Y_{stru} on PSNR-*u*, SSIM-*u*, and HDR-VDP-2. It indicates that the two components are complementary and

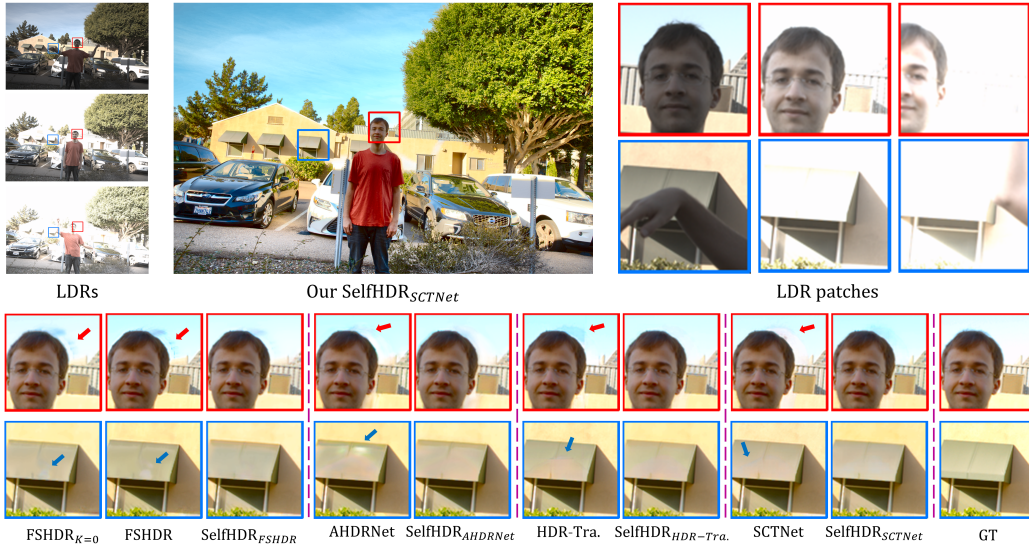
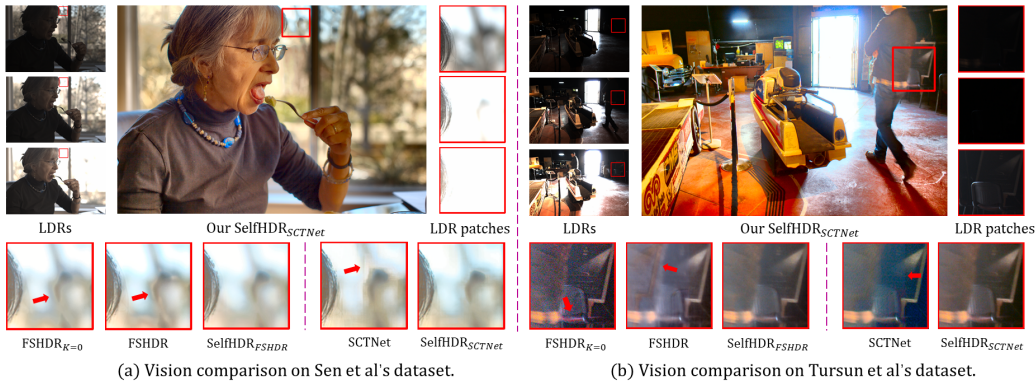


Figure 3: Visual comparison on Kalantari *et al.* dataset (Kalantari *et al.*, 2017). Red and blue arrows indicate areas with ghosting artifacts from other methods. ‘HDR-Tra.’ denotes HDR-Transformer.



(a) Vision comparison on Sen *et al.*'s dataset.

(b) Vision comparison on Tursun *et al.*'s dataset.

Figure 4: Visual comparison on (a) Sen *et al.* (Sen *et al.*, 2012) and (b) Tursun *et al.* (Tursun *et al.*, 2016) datasets. Red arrows indicate areas with poor quality from other methods.

Table 2: Quantitative results of supervision components and final HDR images.

	PSNR- <i>u</i> / SSIM- <i>u</i>	PSNR- <i>l</i> / SSIM- <i>l</i>	HDR-VDP-2
Color Components \mathbf{Y}_{color}	34.45 / 0.9652	39.01 / 0.9783	58.28
Structure Components \mathbf{Y}_{stru}	43.38 / 0.9891	41.74 / 0.9874	64.48
Final HDR Images	43.68 / 0.9901	41.09 / 0.9873	64.57

taking them as supervision is appropriate and effective. Furthermore, we conduct the following two experiments to further illustrate the effectiveness.

Comparison with Component Fusion. It may be a more natural idea to obtain HDR results by fusing the color and structure components. Here we implement that by calculating $M_{color} \mathbf{Y}_{color} + (1 - M_{color}) \mathbf{Y}_{stru}$. We empirically re-adjust the hyperparameter σ_{color} in Eqn. (14), but find it gets the best results when $M_{color} = 0$. In other words, it is difficult to achieve better results by fusing two components simply. Instead, our SelfHDR provides a more flexible and efficient way.

Refining Structure Component. Denote $\hat{\mathbf{Y}}^*$ by the reconstruction network output when inputting multi-exposure images aligned by optical flow (Liu *et al.*, 2009). From another point of view, $\hat{\mathbf{Y}}^*$ can be regarded as a refined structure component with higher quality. Thus, we further take \mathbf{Y}_{color} and $\hat{\mathbf{Y}}^*$ as new supervisions to re-train a reconstruction model, while the performance does not improve. It demonstrates that \mathbf{Y}_{stru} generated by structure-focused network is already sufficient.

Table 3: Effect of loss terms (\mathcal{L}_{se} and \mathcal{L}_{sp}) when training structure-focused network.

$\mathcal{L}_{se} / \mathcal{L}_{sp}$	Y_{stru}		\hat{Y}	
	PSNR- <i>u</i> / PSNR- <i>l</i>			
× / ✓	38.24 / 33.61	38.79 / 33.72		
✓ / ×	42.69 / 41.89	43.09 / 41.13		
✓ / ✓	43.38 / 41.74	43.68 / 41.09		

Table 4: Effect of different M_{color} when training reconstruction network.

M_{color}	\hat{Y}	
	PSNR- <i>u</i> / PSNR- <i>l</i>	PSNR- <i>u</i> / PSNR- <i>l</i>
×	43.55 / 41.12	
Eqn. (9)	43.59 / 41.02	
Eqn. (14)	43.68 / 41.09	

Table 5: Effect of the designed masks (M_{se} and M_{sp}) when training structure-focused network.

M_{se} / M_{sp}	Y_{stru}		\hat{Y}	
	PSNR- <i>u</i> / PSNR- <i>l</i>			
× / ×	38.26 / 33.68	38.82 / 33.71		
✓ / ×	38.29 / 33.65	38.86 / 33.82		
× / ✓	43.26 / 41.73	43.60 / 41.07		
✓ / ✓	43.38 / 41.74	43.68 / 41.09		

Table 6: Effect of pre-alignment processing when constructing Y_{color} and Y_{stru} .

Y_{color} / Y_{stru}	\hat{Y}	
	PSNR- <i>u</i> / PSNR- <i>l</i>	PSNR- <i>u</i> / PSNR- <i>l</i>
× / ×	35.50 / 34.95	
× / ✓	41.66 / 40.90	
✓ / ×	43.41 / 40.76	
✓ / ✓	43.68 / 41.09	

5.2 EFFECT OF LOSS TERMS AND MASKS

Structure-Focused Network. The structure-focused network is trained with the supervision of color component and input reference, implementing by calculating structure-expansion loss \mathcal{L}_{se} and structure-preserving loss \mathcal{L}_{sp} , respectively. Here we explore the effect of different supervisions by using \mathcal{L}_{sp} or \mathcal{L}_{se} only. From Table 3, it can be seen that \mathcal{L}_{sp} may play a weaker role, as it mainly constrains the well-exposed areas whose structure may be also fine in Y_{color} . Nevertheless, combining two supervisions is more favorable than using one, thus both are indispensable.

Moreover, we conduct ablation experiments on the designed masks (M_{sp} and M_{se}) in loss terms. The results in Table 5 show that the masks are competent in avoiding harmful information from supervision. The visualizations of the masks are given in the appendix.

Reconstruction Network. For training the reconstruction network, the adverse effect of ghosting regions from color supervision Y_{color} needs to be avoided as well. We utilize structure component to design a more accurate mask in Eqn. (14), and it does show better results than Eqn. (9) from Table 4.

5.3 EFFECT OF OPTICAL FLOW PRE-ALIGNMENT

When constructing color and structure supervisions, the inputs need to be pre-aligned by the optical flow approach. Here we remove the pre-alignment processing separately to investigate its impact on the final HDR results, which are shown in Table 6. From the table, pre-alignment during obtaining Y_{color} is crucial, and pre-alignment during obtaining Y_{stru} can further improve performance. The corresponding quantitative results of Y_{color} and Y_{stru} can be seen in the appendix.

6 CONCLUSION

By exploiting the internal properties of multi-exposure images, we propose a self-supervised high dynamic range (HDR) reconstruction method named SelfHDR for dynamic scenes. In SelfHDR, the reconstruction network is learned under the supervision of two complementary components, which focus on the color and structure of HDR images, respectively. The color components are synthesized by merging aligned multi-exposure images. The structure components are constructed by feeding aligned inputs into the structure-focused network, which is trained with the supervision of color components and input reference images. Experiments show that SelfHDR outperforms the state-of-the-art self-supervised methods, and achieves comparable results to supervised ones.

REFERENCES

- Guanying Chen, Chaofeng Chen, Shi Guo, Zhetong Liang, Kwan-Yee K Wong, and Lei Zhang. Hdr video reconstruction: A coarse-to-fine network and a real-world benchmark dataset. In *ICCV*, 2021.
- Paul E Debevec and Jitendra Malik. Recovering high dynamic range radiance maps from photographs. In *ACM SIGGRAPH*, 2008.
- Alexey Dosovitskiy, Lucas Beyer, Alexander Kolesnikov, Dirk Weissenborn, Xiaohua Zhai, Thomas Unterthiner, Mostafa Dehghani, Matthias Minderer, Georg Heigold, Sylvain Gelly, et al. An image is worth 16x16 words: Transformers for image recognition at scale. In *ICLR*, 2020.
- Ben Fei, Zhaoyang Lyu, Liang Pan, Junzhe Zhang, Weidong Yang, Tianyue Luo, Bo Zhang, and Bo Dai. Generative diffusion prior for unified image restoration and enhancement. In *CVPR*, 2023.
- Kaiming He, Xiangyu Zhang, Shaoqing Ren, and Jian Sun. Deep residual learning for image recognition. In *CVPR*, 2016.
- Jonathan Ho, Ajay Jain, and Pieter Abbeel. Denoising diffusion probabilistic models. *NeurIPS*, 2020.
- Jun Hu, Orazio Gallo, Kari Pulli, and Xiaobai Sun. Hdr deghosting: How to deal with saturation? In *CVPR*, 2013.
- Xin Huang, Qi Zhang, Ying Feng, Hongdong Li, Xuan Wang, and Qing Wang. Hdr-nerf: High dynamic range neural radiance fields. In *CVPR*, 2022.
- Kim Jun-Seong, Kim Yu-Ji, Moon Ye-Bin, and Tae-Hyun Oh. Hdr-plenoxels: Self-calibrating high dynamic range radiance fields. In *ECCV*, 2022.
- Nima Khademi Kalantari, Ravi Ramamoorthi, et al. Deep high dynamic range imaging of dynamic scenes. *ACM TOG*, 2017.
- Diederik P Kingma and Jimmy Ba. Adam: A method for stochastic optimization. In *ICLR*, 2015.
- Chul Lee, Yuelong Li, and Vishal Monga. Ghost-free high dynamic range imaging via rank minimization. *IEEE signal processing letters*, 2014.
- Jingyun Liang, Jiezhong Cao, Guolei Sun, Kai Zhang, Luc Van Gool, and Radu Timofte. Swinir: Image restoration using swin transformer. In *ICCV*, 2021.
- Ce Liu et al. *Beyond pixels: exploring new representations and applications for motion analysis*. PhD thesis, Massachusetts Institute of Technology, 2009.
- Shuaizheng Liu, Xindong Zhang, Lingchen Sun, Zhetong Liang, Hui Zeng, and Lei Zhang. Joint hdr denoising and fusion: A real-world mobile hdr image dataset. In *CVPR*, 2023.
- Ze Liu, Yutong Lin, Yue Cao, Han Hu, Yixuan Wei, Zheng Zhang, Stephen Lin, and Baining Guo. Swin transformer: Hierarchical vision transformer using shifted windows. In *ICCV*, 2021.
- Zhen Liu, Yinglong Wang, Bing Zeng, and Shuaicheng Liu. Ghost-free high dynamic range imaging with context-aware transformer. In *ECCV*, 2022.
- Kede Ma, Hui Li, Hongwei Yong, Zhou Wang, Deyu Meng, and Lei Zhang. Robust multi-exposure image fusion: a structural patch decomposition approach. *IEEE TIP*, 2017.
- Rafał Mantiuk, Kil Joong Kim, Allan G Rempel, and Wolfgang Heidrich. Hdr-vdp-2: A calibrated visual metric for visibility and quality predictions in all luminance conditions. *ACM TOG*, 2011.
- Tom Mertens, Jan Kautz, and Frank Van Reeth. Exposure fusion: A simple and practical alternative to high dynamic range photography. In *Computer Graphics Forum*, 2009.
- B Mildenhall, PP Srinivasan, M Tancik, JT Barron, R Ramamoorthi, and R Ng. Nerf: Representing scenes as neural radiance fields for view synthesis. In *ECCV*, 2020.

-
- Ben Mildenhall, Peter Hedman, Ricardo Martin-Brualla, Pratul P Srinivasan, and Jonathan T Barron. Nerf in the dark: High dynamic range view synthesis from noisy raw images. In *CVPR*, 2022.
- Michal Nazarczuk, Sibi Catley-Chandar, Ales Leonardis, and Eduardo Pérez Pellitero. Self-supervised hdr imaging from motion and exposure cues. *arXiv preprint arXiv:2203.12311*, 2022.
- Yuzhen Niu, Jianbin Wu, Wenxi Liu, Wenzhong Guo, and Rynson WH Lau. Hdr-gan: Hdr image reconstruction from multi-exposed ldr images with large motions. *IEEE TIP*, 2021.
- Tae-Hyun Oh, Joon-Young Lee, Yu-Wing Tai, and In So Kweon. Robust high dynamic range imaging by rank minimization. *IEEE TPAMI*, 2014.
- K Ram Prabhakar, Rajat Arora, Adhitya Swaminathan, Kunal Pratap Singh, and R Venkatesh Babu. A fast, scalable, and reliable dehazing method for extreme exposure fusion. In *ICCP*, 2019.
- K Ram Prabhakar, Gowtham Senthil, Susmit Agrawal, R Venkatesh Babu, and Rama Krishna Sai S Gorthi. Labeled from unlabeled: Exploiting unlabeled data for few-shot deep hdr dehazing. In *CVPR*, 2021.
- Pradeep Sen, Nima Khademi Kalantari, Maziar Yaesoubi, Soheil Darabi, Dan B Goldman, and Eli Shechtman. Robust patch-based hdr reconstruction of dynamic scenes. *ACM TOG*, 2012.
- Karen Simonyan and Andrew Zisserman. Very deep convolutional networks for large-scale image recognition. In *ICLR*, 2015.
- Jiaming Song, Chenlin Meng, and Stefano Ermon. Denoising diffusion implicit models. In *ICLR*, 2021.
- Jou Won Song, Ye-In Park, Kyeongbo Kong, Jaeho Kwak, and Suk-Ju Kang. Selective transhdr: Transformer-based selective hdr imaging using ghost region mask. In *ECCV*, 2022.
- Steven Tel, Zongwei Wu, Yulun Zhang, Barthélemy Heyrman, Cédric Demonceaux, Radu Timofte, and Dominique Ginhac. Alignment-free hdr dehazing with semantics consistent transformer. In *ICCV*, 2023.
- A TOMASZEWSKA. Image registration for multi-exposure high dynamic range image acquisition. In *Proceedings of International Conference in Central Europe on Computer Graphics, Visualization and Computer Vision (WSCG)*, 2007.
- Okan Tarhan Tursun, Ahmet Oğuz Akyüz, Aykut Erdem, and Erkut Erdem. An objective dehazing quality metric for hdr images. In *Computer Graphics Forum*. Wiley Online Library, 2016.
- Lin Wang and Kuk-Jin Yoon. Deep learning for hdr imaging: State-of-the-art and future trends. *IEEE TPAMI*, 2021.
- Zhou Wang, Alan C Bovik, Hamid R Sheikh, and Eero P Simoncelli. Image quality assessment: from error visibility to structural similarity. *IEEE TIP*, 2004.
- Shangzhe Wu, Jiarui Xu, Yu-Wing Tai, and Chi-Keung Tang. Deep high dynamic range imaging with large foreground motions. In *ECCV*, 2018.
- Qingsen Yan, Jinqiu Sun, Haisen Li, Yu Zhu, and Yanning Zhang. High dynamic range imaging by sparse representation. *Neurocomputing*, 2017.
- Qingsen Yan, Dong Gong, Qinfeng Shi, Anton van den Hengel, Chunhua Shen, Ian Reid, and Yanning Zhang. Attention-guided network for ghost-free high dynamic range imaging. In *CVPR*, 2019a.
- Qingsen Yan, Yu Zhu, and Yanning Zhang. Robust artifact-free high dynamic range imaging of dynamic scenes. *Multimedia Tools and Applications*, 2019b.
- Qingsen Yan, Weiye Chen, Song Zhang, Yu Zhu, Jinqiu Sun, and Yanning Zhang. A unified hdr imaging method with pixel and patch level. In *CVPR*, 2023a.
- Qingsen Yan, Song Zhang, Weiye Chen, Hao Tang, Yu Zhu, Jinqiu Sun, Luc Van Gool, and Yanning Zhang. Smae: Few-shot learning for hdr dehazing with saturation-aware masked autoencoders. In *CVPR*, 2023b.
- Wei Zhang and Wai-Kuen Cham. Gradient-directed multiexposure composition. *IEEE TIP*, 2011.

APPENDIX

The content of the appendix material involves:

- Analysis and visualization of masks in Sec. **A**.
- Additional results on effect of optical flow alignment in Sec. **B**.
- Ablation study on adjusting σ_{se} and σ_{color} in Sec. **C**.
- Additional qualitative comparisons in Sec. **D**.

A ANALYSIS AND VISUALIZATION OF MASKS

In order to avoid harmful information in supervision during training structure-focused network, we carefully design the mask M_{sp} and M_{se} for calculating structure-preserving loss \mathcal{L}_{sp} and structure-expansion loss \mathcal{L}_{se} , respectively. The quantitative results of related ablation experiments are shown in Table 5. Here we give more analysis about the elaborate masks and visualize an example in Fig. A. Therein, the corresponding color component is shown in Fig. A (g).

Mask M_{sp} in Structure-Preserving Loss. The structure-preserving loss aims at guiding the network to preserve textures of the input reference image, and it is calculated between model output and linear medium-exposure image H_2 . From Table 5, it leads to poor performance when measuring the distance between the two directly, as the structural information of dark and over-exposed regions is incomplete in medium-exposure image H_2 .

Thus, we suggest embedding a mask M_{sp} into the loss, and it should emphasize the well-exposed areas and mitigate the adverse effects of dark as well as over-exposed areas. $\Lambda_2(I_2)$ in Fig. 1 can do just that, and we adopt it as M_{sp} . The visualization of a $\Lambda_2(I_2)$ example is shown in Fig. A (i). It can be seen that the overexposed area surrounded by the blue box is successfully suppressed.

Mask M_{se} in Structure-Expansion Loss. The structure-expansion loss aims at guiding the network to learn textures from non-reference inputs, and it is calculated between model output and color component Y_{color} . As Y_{color} is obtained by fusing aligned multi-exposure images (see Fig. A (b), (e), and (f)), it is inevitable that ghosting artifacts exist in Y_{color} (see the area surrounded by the red box in Fig. A (g)) when the alignment fails.

Thus, a mask M_{se} should be designed to circumvent the adverse effects of these ghosting areas for better guiding the network. It is not appropriate to calculate the mask based on the simple difference between Y_{color} and reference image H_2 . Because even if the dark and over-exposed areas are aligned well, the difference between Y_{color} and H_2 is still large (see the area surrounded by the blue box in Fig. A (j)). As a result, we utilize $\Lambda_2(I_2)$ again to mitigate the adverse effects of these areas. Specifically, we multiply $\Lambda_2(I_2)$ to Y_{color} and H_2 for calculating the difference, as shown in Eqn. (9). A mask example is shown in Fig. A (k). It can be seen that the well-aligned over-exposed areas surrounded by the blue box are successfully retained, and only the misaligned area is masked.

With the designed masks, the generated structure component Y_{stru} in Fig. A (l) combines the strengths of the supervisions Y_{color} and H_2 , while discarding their weaknesses.

B ADDITIONAL RESULTS ON EFFECT OF OPTICAL FLOW ALIGNMENT

When constructing color and structure supervisions, the inputs need to be pre-aligned by the optical flow approach (Liu et al., 2009). We remove the pre-alignment processing separately to investigate its impact on the final HDR results, which are shown in Table A. From the table, the pre-alignment during obtaining Y_{color} is crucial, as Y_{color} affects the quality of Y_{stru} , while Y_{color} and Y_{stru} decide the final HDR result. On this basis, pre-alignment during generating Y_{stru} can further improve performance, achieving 0.27 dB PSNR gain on the HDR result \hat{Y} .

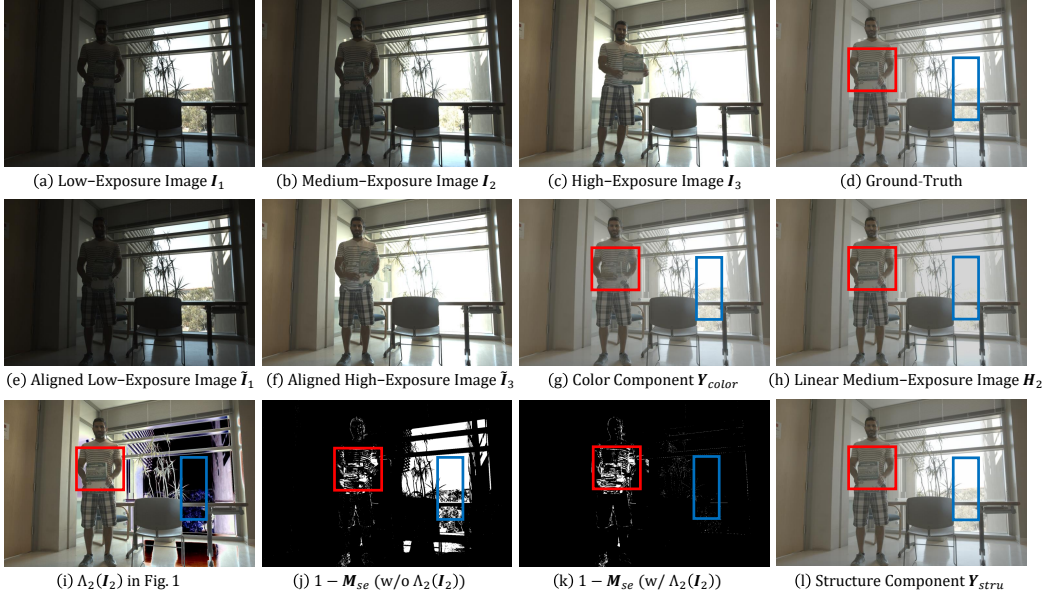


Figure A: Visualization of masks and related images. (a)~(c) show the multi-exposure images, while (d) is the corresponding ground-truth from Kalantari *et al.* (Kalantari *et al.*, 2017) dataset. (e) and (f) show the aligned low-exposure and aligned high-exposure images, respectively, which are obtained by optical flow (Liu *et al.*, 2009) alignment with the reference of medium-exposure image. (g) is the constructed color component by fusing aligned multi-exposure images. (h) is the medium-exposure image in the linear domain. (i) is the mask as a blending weight in Fig. 1. (j) and (k) denote the masks $1 - M_{se}$ (see Eqn. (9)) constructed without and with $\Lambda_2(I_2)$, respectively. (l) is the generated structure component. The red box indicates the area where optical flow alignment fails, and the blue box indicates the area with high brightness.

Table A: Effect of pre-alignment processing when constructing supervision information (Y_{color} and Y_{stru}). The final HDR results (\hat{Y}) are obtained by learning the model with corresponding (Y_{color} and Y_{stru}) supervisions.

	Y_{color}	Y_{stru}	Y_{color} PSNR- <i>u</i> / PSNR- <i>l</i>	Y_{stru} PSNR- <i>u</i> / PSNR- <i>l</i>	\hat{Y} PSNR- <i>u</i> / PSNR- <i>l</i>
Pre-Alignment	×	×	25.69 / 31.31	34.58 / 34.35	35.50 / 34.95
Processing	×	✓	25.69 / 31.31	39.04 / 40.38	41.66 / 40.90
	✓	×	34.45 / 39.01	43.07 / 40.45	43.41 / 40.76
	✓	✓	34.45 / 39.01	43.38 / 41.74	43.68 / 41.09

Table B: Effect of σ_{se} in Eqn. (9).

σ_{se}	Y_{stru} PSNR- <i>u</i> / PSNR- <i>l</i>	\hat{Y} PSNR- <i>u</i> / PSNR- <i>l</i>
2.5/255	43.27 / 41.49	43.64 / 40.88
5/255	43.38 / 41.74	43.68 / 41.09
7.5/255	43.18 / 41.67	43.57 / 41.04

Table C: Effect of σ_{color} in Eqn. (14).

σ_{color}	\hat{Y} PSNR- <i>u</i> / PSNR- <i>l</i>
5/255	43.60 / 41.08
10/255	43.68 / 41.09
15/255	43.61 / 41.10

C ABLATION STUDY ON ADJUSTING σ_{se} AND σ_{color}

The hyperparameters σ_{se} (see Eqn. (9)) and σ_{color} (see Eqn. (14)) are set to 5/255 and 10/255 by default for experiments, respectively. Here, we vary σ_{se} or σ_{color} to conduct experiments. Table B and C show the experimental results, respectively. The results show that the sensitivity σ_{se} and σ_{color} of our SelfHDR is acceptable.

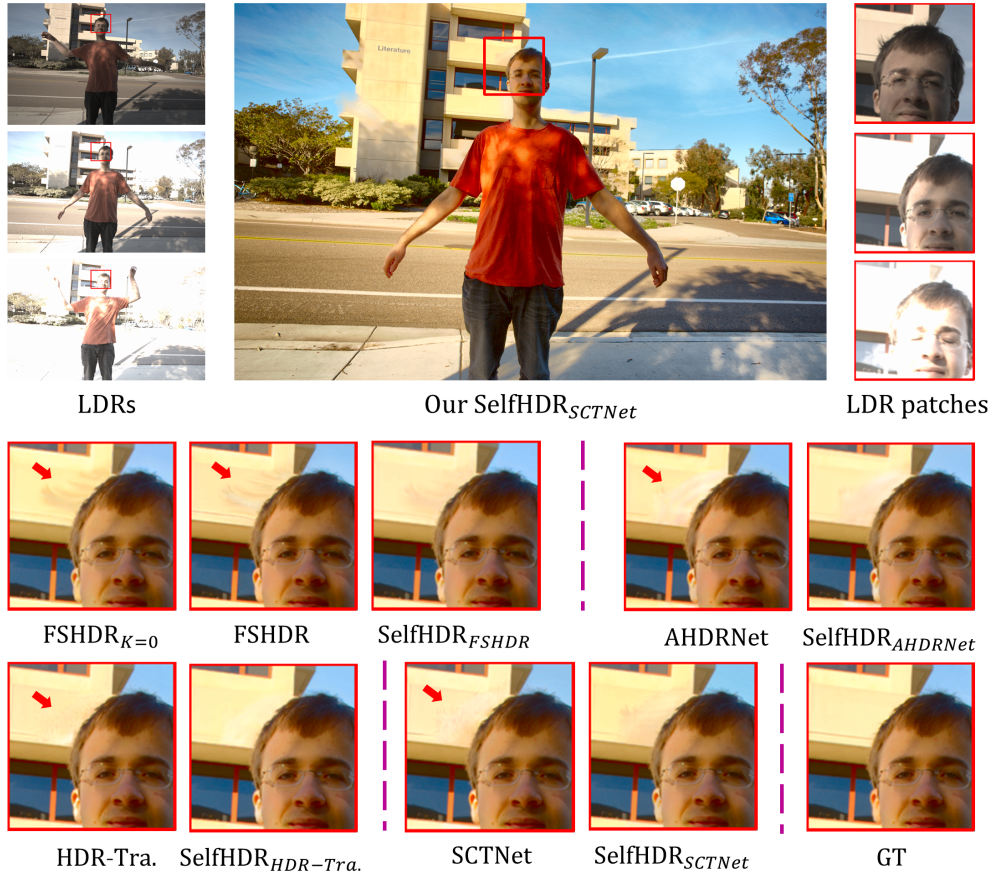


Figure B: Visual comparison on Kalantari *et al.* dataset (Kalantari *et al.*, 2017). Red arrows indicate areas with ghosting artifacts from other methods. ‘HDR-Tra.’ denotes HDR-Transformer.

D ADDITIONAL QUALITATIVE COMPARISONS

Additional visual comparisons on Kalantari *et al.* (Kalantari *et al.*, 2017) dataset are shown in Fig. B and Fig. C, respectively. Our SelfHDR has fewer ghosting artifacts than zero-shot FSHDR (*i.e.*, FSHDR _{$K=0$}) (Prabhakar *et al.*, 2021). Sometimes, SelfHDR even outperforms the corresponding supervised methods. Red arrows in the results indicate areas with ghosting artifacts in other methods.

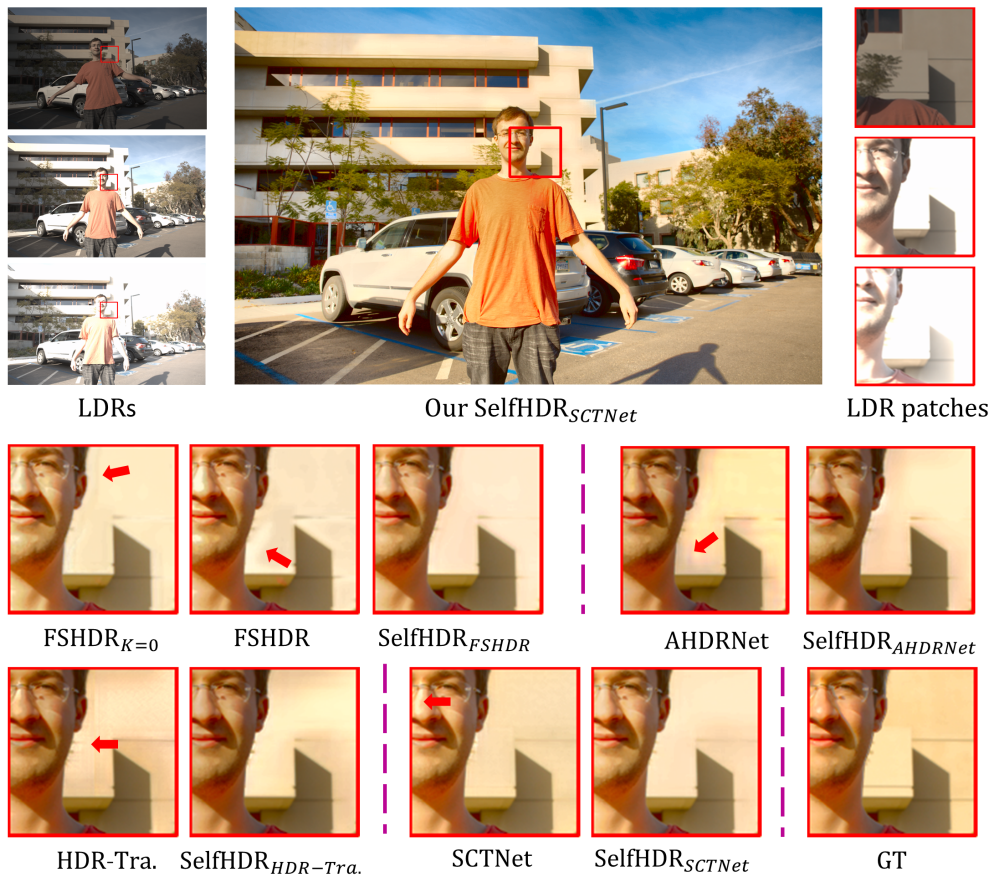


Figure C: Visual comparison on Kalantari *et al.* dataset (Kalantari *et al.*, 2017). Red arrows indicate areas with ghosting artifacts from other methods. ‘HDR-Tra.’ denotes HDR-Transformer.